



## Full Length Article

# High-performance supercapacitors using flexible and freestanding MnO<sub>x</sub>/carbamide carbon nanofibers



Edmund Samuel<sup>a,1</sup>, Hong Seok Jo<sup>a,1</sup>, Bhavana Joshi<sup>a</sup>, Hyun Goo Park<sup>a</sup>, Yong Il Kim<sup>a</sup>, Seongpil An<sup>a</sup>, Mark T. Swihart<sup>b</sup>, Je Moon Yun<sup>c</sup>, Kwang Ho Kim<sup>c,d,\*\*</sup>, Sam S. Yoon<sup>a,\*</sup>

<sup>a</sup> School of Mechanical Engineering, Korea University, Seoul 024841, Republic of Korea

<sup>b</sup> Department of Chemical & Biological Engineering, University at Buffalo, The State University of New York, Buffalo, NY 14260–4200, USA

<sup>c</sup> Global Frontier R&D Center for Hybrid Interface Materials, Pusan National University, San 30 Jangjeon-dong, Geumjeong-gu, Busan 609–735, Republic of Korea

<sup>d</sup> School of Materials Science and Engineering, Pusan National University, San 30 Jangjeon-dong, Geumjeong-gu, Busan 609–735, Republic of Korea

## ARTICLE INFO

## Article history:

Received 29 March 2017

Received in revised form 26 May 2017

Accepted 7 June 2017

Available online 13 June 2017

## Keywords:

Electrospinning

MnO<sub>x</sub>/CCNF

Flexible

Supercapacitor

## ABSTRACT

We demonstrate the fabrication of a MnO<sub>x</sub>/carbamide carbon nanofiber (CCNF) composite consisting of MnO particles embedded in CCNFs as a highly flexible and freestanding electrode material for supercapacitors. A sacrificial polymer component, polymethylmethacrylate, included in the precursor solution, pyrolyzes during heating, resulting in pores in the fibers, some of which are filled by the MnO nanocrystals. Carbamide is added to control the size of the MnO<sub>x</sub> particles as well as to increase the carbon content of the composite and hence its conductivity. The X-ray diffraction and Raman spectra of the composite show that the MnO particles formed have low crystallinity. Transmission electron microscopy confirms that the MnO particles are distributed very uniformly over the CCNFs. Symmetric supercapacitors constructed using electrodes of this composite exhibit specific capacitances of 498 F.g<sup>-1</sup> at a scan rate of 10 mV.s<sup>-1</sup> and 271 F.g<sup>-1</sup> at a current density of 1 A.g<sup>-1</sup>. They also exhibit excellent long-term cycling performance, retaining 93% of their initial capacity after 5000 cycles of galvanostatic charging/discharging.

© 2017 Elsevier B.V. All rights reserved.

## 1. Introduction

Supercapacitors (SCs) show high power density, superior cycling performance, and high charge/discharge rates and are ideal for use in portable energy devices that must provide a high power density for brief periods of time [1,2]. This is because SCs exhibit power densities greater than those of rechargeable ion-batteries and energy densities much higher than those of conventional electrolytic capacitors [3]. In carbon-based SCs, the energy storage mechanism involves the electrostatic adsorption of ions at the electrolyte/electrode interface. That is to say, it is based on the electrical double layer capacitance (EDLC) [4,5]. The total energy density of SCs can be improved by adding nanoparticles of an electrochemically active metal oxide that exhibits pseudocapacitance owing to fast and reversible Faradaic reactions at the particle surfaces [6].

\* Corresponding author.

\*\* Corresponding author.

E-mail addresses: [kwhokim@pusan.ac.kr](mailto:kwhokim@pusan.ac.kr) (K.H. Kim), [skyoonyoon@korea.ac.kr](mailto:skyoonyoon@korea.ac.kr),

[skyoonyoonyoung@gmail.com](mailto:skyoonyoonyoung@gmail.com) (S.S. Yoon).

<sup>1</sup> These authors have contributed equally.

The first oxide whose pseudocapacitance characteristics studied was RuO<sub>2</sub> [7,8]. Since then, the pseudocapacitances of other metal oxides such as Fe<sub>2</sub>O<sub>3</sub>, SnO<sub>2</sub>, MnO, and WO<sub>3</sub> have also been investigated [4,9–11]. However, most of these metal oxides show low electrical conductivity [4,7]. To overcome this issue, researchers have combined the metal oxides with various carbon materials, such as graphene, reduced graphene oxide, carbon nanotubes (CNTs), and carbon nanofibers (CNFs), to create nanocomposites that exhibit both pseudocapacitance and high conductivity. The electrospinning and subsequent carbonization of solutions of polyacrylonitrile (PAN) and salts or nanoparticles of the metal in question can yield metal oxide/CNF composites with desirable properties such as high conductivity and flexibility [12]. The synergistic effects of the EDLC and pseudocapacitance in these nanocomposites result in a high specific capacitance even at high charge/discharge rates [4,13,14].

Manganese oxide is a good candidate for forming composite materials for SC electrodes because of its excellent pseudocapacitance characteristics, high abundance, low cost (compared to RuO<sub>2</sub>), environmentally friendly nature, and compatibility with aqueous electrolytes [15]. As noted above, the low conductivity of manganese oxide (MnO<sub>x</sub>) can be circumvented by combining

**Table 1**  
Precursor composition.

Case	MnAc (wt.%)
MnO-1	1
MnO-2	2
MnO-3	4

it with carbon materials. Wang et al. [16] incorporated  $\text{MnO}_x$  and CNTs into CNFs; the formed composite exhibited a specific capacitance of  $374 \text{ F}\cdot\text{g}^{-1}$  at a scan rate of  $2 \text{ mV}\cdot\text{s}^{-1}$ . Similarly, Cai et al. [5] fabricated a porous CNF/ $\text{MnO}_x$  composite by electrospinning. However, while both groups stated that their electrode materials were freestanding, the flexibilities of the fabricated electrodes were not mentioned. Yang et al. [17] performed electrochemical measurements on a composite formed by loading manganese oxide on a vitreous carbon disk. Nie et al. [18] synthesized a composite electrode material by loading a large amount of  $\text{MnO}_2$  on carbonaceous spheres. However, the cyclic voltammetry (CV) curves of the composite contained peaks indicative of irreversible redox reactions. Furthermore, the composite exhibited low capacitance retention, showing just 60% of the initial capacitance after 500 cycles. Moreover, most of the aforementioned fabrication processes involve multiple steps, which adds to the cost and complexity of large-scale production.

Carbamide has been used as a nitrogen dopant for CNFs as well as a structure-directing agent [19,20]. For instance, Chen et al. [21] controlled the morphology of ZnCo-oxide particles using carbamide to produce core-shell structures. Based on these reports, we hypothesized that carbamide could be used to control the morphology of  $\text{MnO}_x$  crystals formed using manganese acetate (MnAc) as the precursor. Furthermore, polymethylmethacrylate (PMMA) was used as a sacrificial polymer, which decomposed during the carbonization (high-temperature annealing in an inert gas atmosphere) process [22,23]. Therefore, in this study, we combined the sacrificial agent PMMA and carbamide with PAN to produce carbamide CNFs (CCNFs) through electrospinning. This yielded CCNFs with an increased specific capacitance. No additional activation process was necessary to form the CCNFs. Further, the CCNFs showed pseudocapacitive characteristics because of the added MnAc, which formed  $\text{MnO}_x$  particles during the annealing process. Finally, we observed that the resulting flexible, freestanding, and binder-free  $\text{MnO}_x$ /CCNF composite exhibited excellent characteristics as an electrode material in symmetric SCs.

## 2. Experimental procedure

We fabricated  $\text{MnO}_x$ /CCNF composite mats by electrospinning, as shown schematically in Fig. 1a. The concentrations of MnAc ( $\text{Mn}(\text{CH}_3\text{COO})_2$ ; 98%, Sigma-Aldrich) used to form the  $\text{MnO}_x$ /CCNF composite are listed in Table 1; samples MnO-1, MnO-2, and MnO-3 correspond to MnAc concentrations of 1, 2, and 4 wt%, respectively, in the precursor solution. Details of the other samples corresponding to lower MnAc concentrations are provided in Supporting Information. To prepare the electrospinning precursor solution, PAN ( $M_w = 150 \text{ kDa}$ ; Sigma-Aldrich; 8 wt%) and PMMA ( $M_w \approx 120 \text{ kDa}$ ; Sigma-Aldrich; 0.4 wt%) were mixed with 4.577 g of *N,N*-dimethylformamide (DMF, 99.8%, Sigma-Aldrich). To ensure a homogeneous solution, the PAN, PMMA, and DMF mixture was stirred at  $60^\circ\text{C}$  [24]. Next, MnAc and carbamide (99%, SAMCHUN, South Korea) were added to the PAN-PMMA/DMF solution, and the solution was stirred for 24 h, yielding the precursor solution to be loaded in the syringe pump, as shown in Fig. 1a.

It was observed that  $\text{MnO}_x$  particles formed when MnAc was added to the PAN-PMMA/DMF solution (see Fig. S1). To prevent this, carbamide and MnAc were added in the same amount to the

PAN-PMMA/DMF solution. However, this resulted in brittle composite nanofibers. Hence, we gradually reduced the concentration of carbamide, in order to determine the optimal concentration for obtaining flexible fibers. The optimal MnAc/carbamide concentration ratio (wt%) was found to be 3:1. Further, the optimized parameters for the electrospinning process were as follows: precursor flow rate of  $500 \mu\text{L}\cdot\text{h}^{-1}$ , voltage of 9–10 kV, and spinning time of 90 min. The needle-to-fiber collector (Al foil) distance was kept at 15 cm, to ensure stable electrospinning. The peeled-off composite fibers were stabilized and carbonized by heating at  $280^\circ\text{C}$  for 30 min and at  $800^\circ\text{C}$  for 60 min, respectively. The ramping rates for the stabilization and carbonization processes were 5 and  $3^\circ\text{C}\cdot\text{min}^{-1}$ , respectively. The carbonized  $\text{MnO}$ /CCNF composite materials were flexible and freestanding, as can be seen from Fig. 1a. A transmission electron microscopy (TEM) image of a  $\text{MnO}$ /CCNF composite after carbonization is shown in Fig. 1b. The electrochemical performances of the  $\text{MnO}$ /CCNF composites were measured using a WBCS3000 battery testing system (WonATech, Seoul, South Korea). Coin cells (CR2032) with two electrodes consisting of the  $\text{MnO}$ /CCNF mats (14 mm in diameter) were prepared. No additional current collector was used. The two electrodes were electrically isolated using a polymer separator (Celgard 3501; Celgard, Chungbuk, South Korea). The electrolyte used was 6 M KOH, and the measurements were performed for voltages of  $-0.3$  to  $0.7 \text{ V}$ . A light-emitting diode (LED) test was performed using two SC cells with dimensions of  $2 \text{ cm} \times 2 \text{ cm}$ , as shown in Fig. 1c. The separator and the electrolyte were sandwiched between the two electrodes.

## 3. Results and discussion

The X-ray diffraction (XRD, SmartLab, Rigaku) patterns of the  $\text{MnO}_x$ /CCNF composite samples obtained after annealing at  $800^\circ\text{C}$  are shown in Fig. 2a. Small peaks can be seen in the case of the samples produced using 1, 2, and 4 wt% MnAc, that is, for samples MnO-1, MnO-2, and MnO-3, respectively. The low intensity of the peaks suggests that the crystallinity of the MnO particles present on the CNFs was low. The peaks were compared with the standard data in the JCPDS database (Card No. 07-0230). The peaks observed at  $2\theta$  values of  $34.9^\circ$ ,  $40.7^\circ$ , and  $58.8^\circ$  correspond to the (111), (200), and (220) planes of MnO, respectively. The XRD peaks and the corresponding planes indicate that MnO exhibited the space group Fm3m. The presence of  $\text{Mn}_3\text{O}_4$  (JCPDS Card No. 24-0734) was confirmed by the presence of the relatively weak peaks at  $32^\circ$  (103) and  $36^\circ$  (211); these peaks are marked with circles. For all the  $\text{MnO}_x$ /CCNF composite samples, the only other peak observed was one related to carbon ( $2\theta = 21.7^\circ$ ). This broad peak corresponds to the turbostratic graphitic phase of carbon and is attributable to the PAN used. The corresponding interplanar spacing was 0.4 nm, which is higher than that for common graphite (0.34 nm,  $26.5^\circ$ ) [25]. This increase in the interlayer spacing is attributable to the low-temperature carbonization process. In general, a higher interlayer spacing means improved electrolyte ion transport and thus a higher capacitive storage capacity [26].

The presence of carbon and  $\text{MnO}_x$  in the composite samples was confirmed by Raman spectroscopy. The results indicated the presence of graphene-like carbon as well as defects in the CNFs. Fig. 2b shows the Raman spectra, obtained using a LabRam ARAMIS IR2 system (HORIBA JOBIN YVON), of the various  $\text{MnO}_x$ /CCNF composite samples. The D band, which is indicative of carbon defects, was recorded at  $1356$ ,  $1361$ , and  $1376 \text{ cm}^{-1}$  in the case of samples MnO-1, MnO-2, and MnO-3, respectively. The G band, which is associated with  $\text{sp}^2$ -conjugated bonds, was observed at  $1586$ ,  $1589$ , and  $1590 \text{ cm}^{-1}$  for MnO-1, MnO-2, and MnO-3, respectively. The shift in D and G bands toward higher wavenumbers is due to an increase in defects and decrease in graphitic carbon content. This suggests that

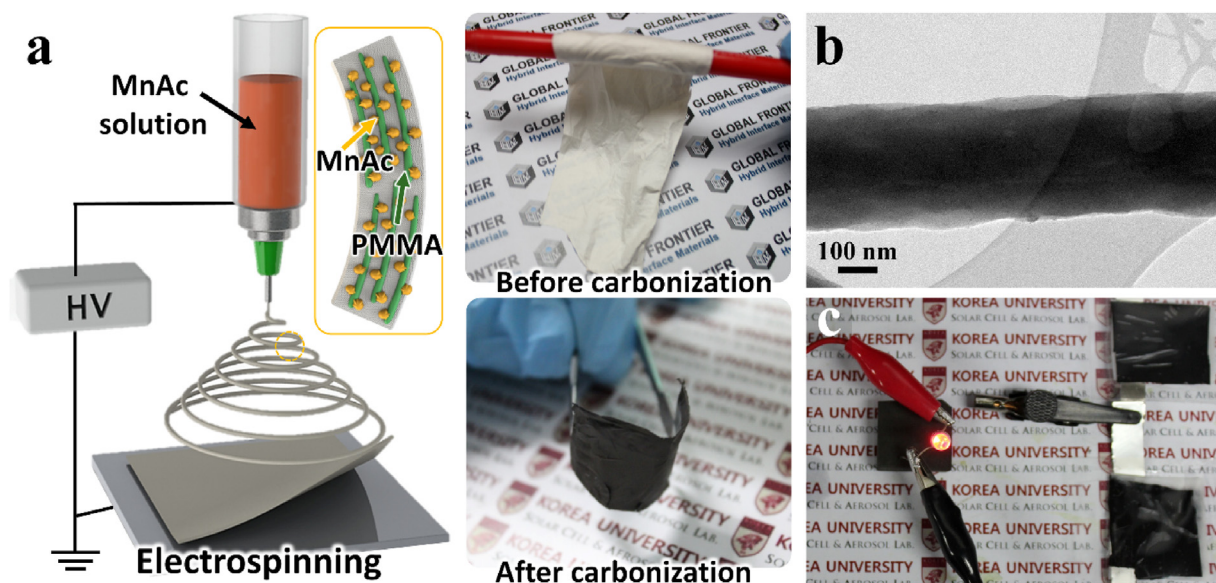


**Fig. 1.** (a) Schematic of electrospinning setup used for synthesizing  $\text{MnO}_x/\text{CCNF}$  composites, (b) TEM image of  $\text{MnO}_x/\text{CCNF}$ , and (c) LED test performed using two flexible symmetric SC cells in series.

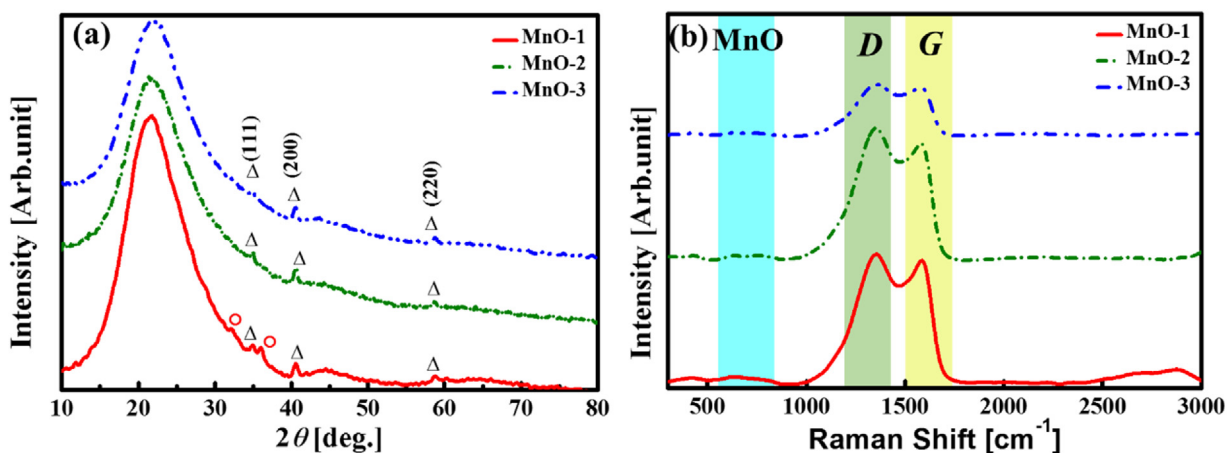


**Fig. 2.** (a) X-ray diffraction patterns and (b) Raman spectra of various  $\text{MnO}_x/\text{CCNF}$  composite samples.

**Table 2**

The comparison of Raman peaks of various MnO samples.

Case	D peak [ $\text{cm}^{-1}$ ]	G peak [ $\text{cm}^{-1}$ ]	$I_D/I_G$
MnO-1	1356	1589	1.033
MnO-2	1361	1557	1.105
MnO-3	1376	1579	1.114

inclusion of a higher amount of MnAc can hinder the formation of defect-free graphene-like carbon [27]. The ratios of the intensities of the D and G bands ( $I_D/I_G$ ) for MnO-1, MnO-2, and MnO-3 were estimated, and the values are listed in Table 2. The  $I_D/I_G$  ratio was higher than unity for all the composite samples, indicating that the composites exhibited a high degree of disorder and poor graphitization. In general, increasing the carbonization temperature reduces the degree of disorder and increases the extent of graphitization of CNFs. However, carbonization at excessively high temperatures can lead to the aggregation of metal particles during the oxygen removal process. This can degrade the electrochemical properties of the material in question [24]. For this reason, the carbonization temperature was limited to 800 °C.

The presence of defective carbon was also confirmed by XRD analysis, as evidenced by the change in the diffraction angle from 25 to 21.7°. Further, a broad peak related to MnO was observed at 600–625  $\text{cm}^{-1}$  in the Raman spectrum (see light-blue region in Fig. 2b), confirming the presence of  $\text{Mn}_3\text{O}_4$  [28], because this peak can be ascribed to the symmetric stretching vibrations of the Mn-O bond. In addition, this peak confirmed the formation of manganese oxide [29]. Overall, the intensities of the MnO peaks were markedly lower than those of the D and G bands because the MnAc content was much lower than the carbon content from PAN.

The surface morphologies of the MnO/CCNF composite samples were studied using scanning electron microscopy (SEM) (FE-SEM, S-5000, Hitachi, Ltd.). Fig. 3 shows low- (upper row) and high-magnification (lower row) SEM images of the samples. An increase in the MnAc concentration resulted in an increase in the surface roughness of the CCNFs. This increase in the roughness was attributed to an increase in the number of carbon defects formed (also see Table 2). However, the images also show that the fabricated nanofibers were uniform in diameter.

Fig. 4a shows the elemental survey spectrum of sample MnO-1 obtained using X-ray photoelectron spectroscopy (XPS, X-TOOL, ULVAC-PHI), which was performed to analyze the compositions of

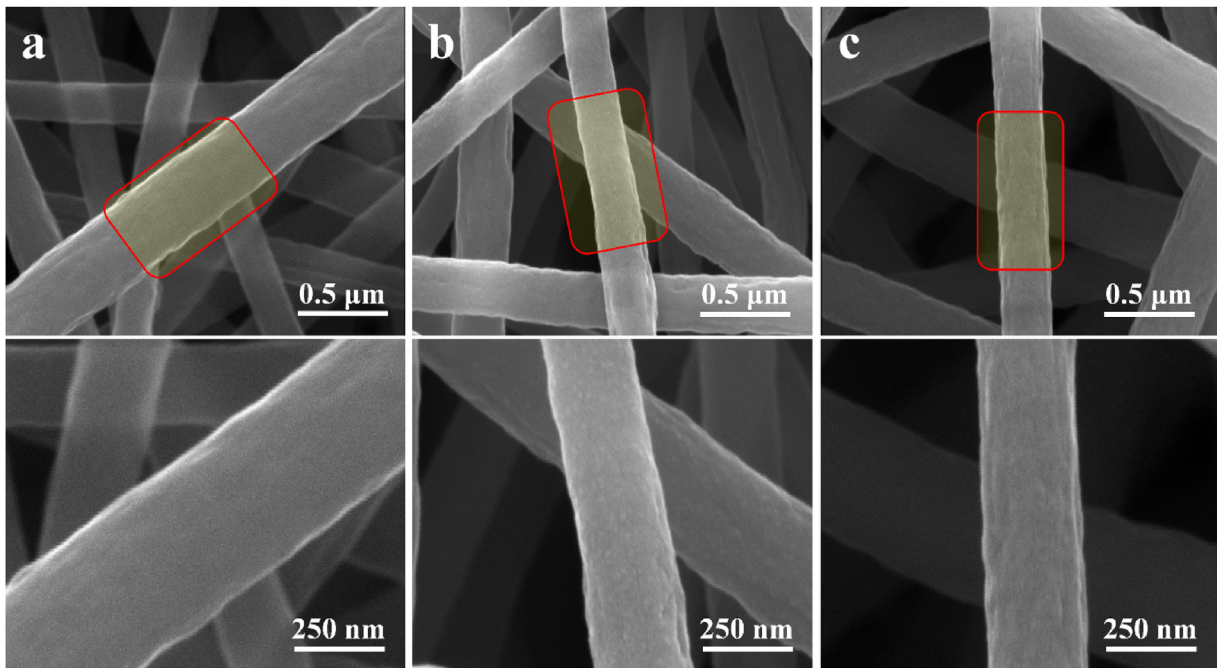


Fig. 3. Low- (upper row) and high-magnification (lower row) SEM images of various MnO/CCNF composite samples: (a) MnO-1 (b) MnO-2, and (c) MnO-3.

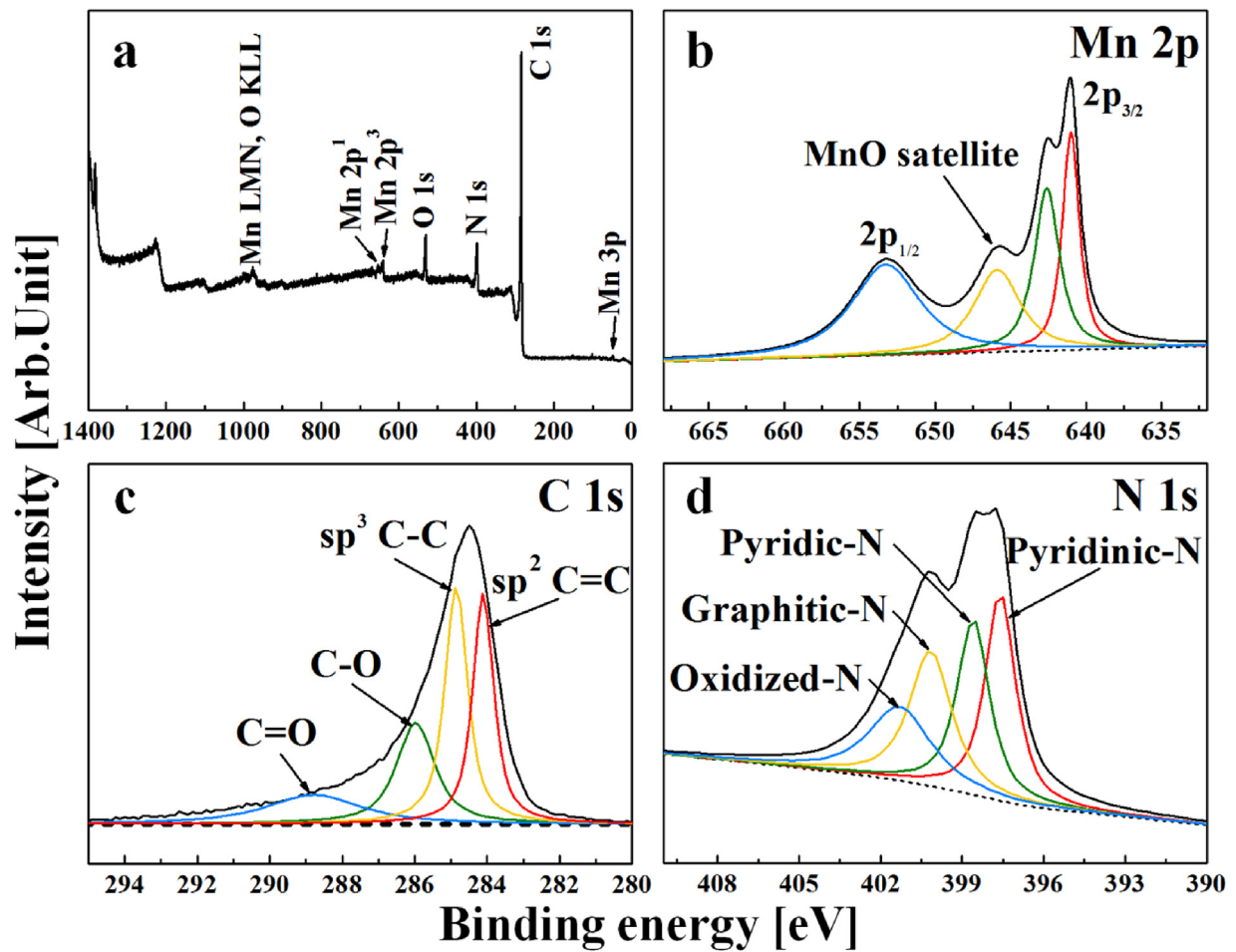


Fig. 4. (a) XPS survey spectra of MnO<sub>x</sub>/CCNF composite sample MnO-1. High-resolution spectra of (b) Mn2p, (c) C1s, and (d) N1s binding energy ranges.

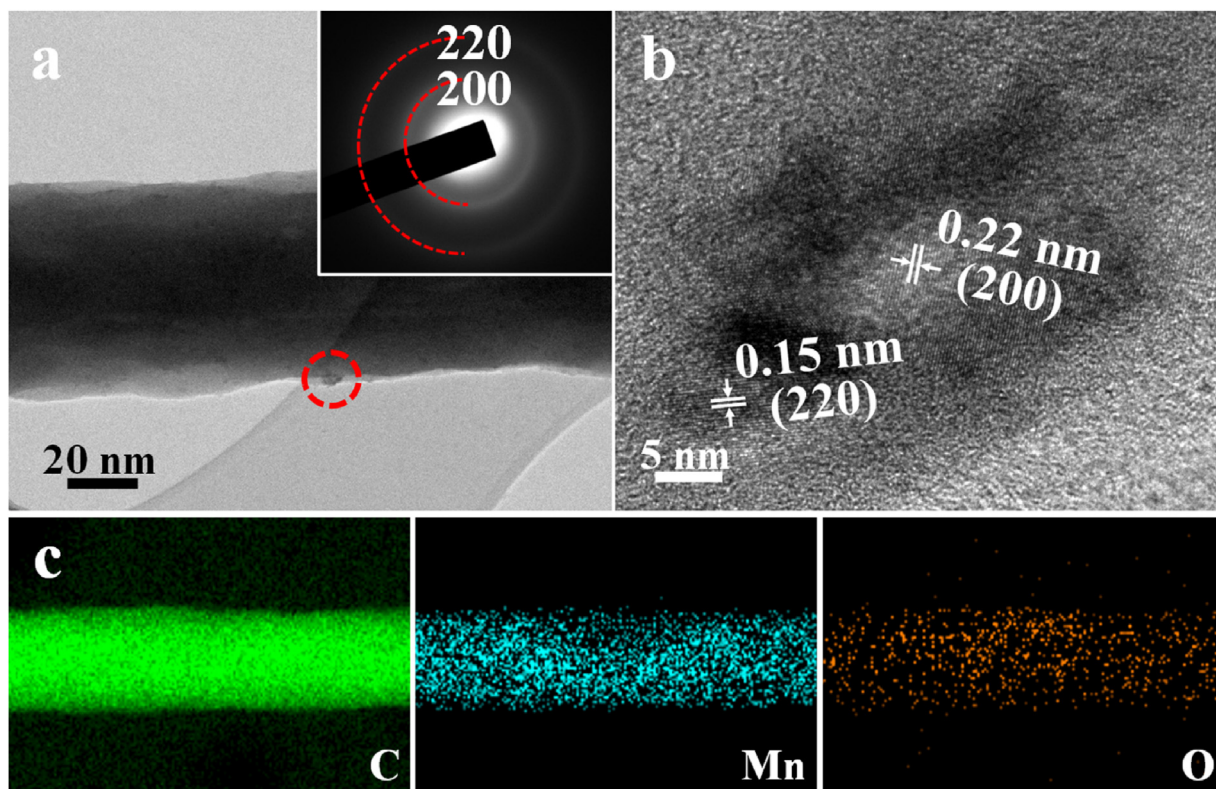


Fig. 5. (a) TEM image of MnO-1 (inset is corresponding SAED pattern), (b) HRTEM image, and (c) elemental maps for C, Mn, and O along a CNF.

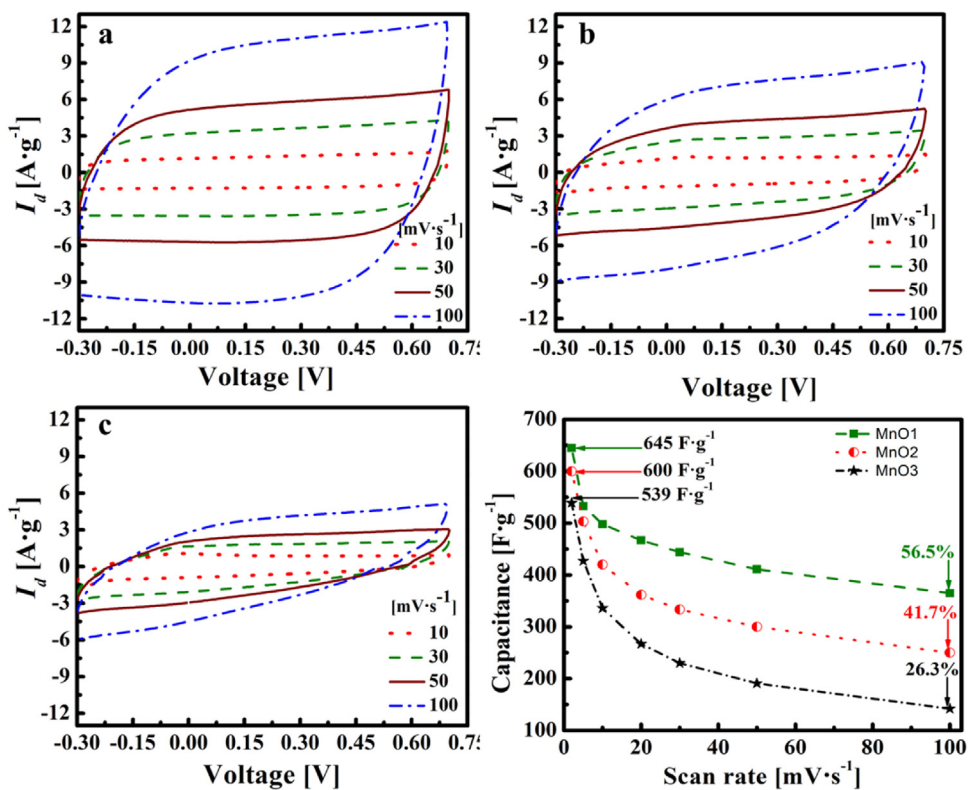


Fig. 6. CV curves of various MnO<sub>x</sub>/CCNF composite electrodes at different scan rates: (a) MnO-1, (b) MnO-2, and (c) MnO-3 and (d) their specific capacitances for scan rates of 2–100 mV·s<sup>-1</sup>.

the composite samples. Fig. 4b–d show the high-resolution core level Mn2p, C1s, and N1s, spectra, respectively. As can be seen from

the Mn2p spectrum in Fig. 4b, the binding energies of the Mn2p<sub>3/2</sub> and Mn2p<sub>1/2</sub> peaks are 641.4 and 653.2 eV, respectively, and their

**Table 3**  
Comparison of specific capacities reported so far with the present study.

Materials	Capacitance [F·g <sup>-1</sup> ]	Scan rate [mV·s <sup>-1</sup> ]	Potential window [V]	Electrolyte	Ref.
MnO <sub>2</sub> /CNT	374	2	0–0.9	0.1 M <sup>a</sup>	[16]
MnO/rGO	52	20	0–1.1	1 M <sup>b</sup>	[32]
MnO/CNF	551	2	–0.1–0.9	–	[35]
MnO <sub>2</sub> core-shell/C	252	2	0–0.8	1 M <sup>a</sup>	[36]
MnO(nanoparticles)/C	100	5	–1.0–0	0.5 M <sup>a</sup>	[3]
MnO <sub>2</sub> /C	252	5	–0.5–0.5	1 M <sup>a</sup>	[37]
MnO nanowire/C	269	10	–0.4–0.7	1 M <sup>a</sup>	[38]
MnO <sub>x</sub> -N—Carbon nanospheres	258	1	–1–0	6 M <sup>c</sup>	[1]
MnO <sub>x</sub> /CNF	200	1	0–0.9	0.5 M <sup>d</sup>	[5]
<b>MnO<sub>x</sub>/CNF</b>	<b>498</b>	<b>10</b>	<b>–0.3–0.7</b>	<b>6 M<sup>c</sup></b>	<b>Present</b>

<sup>a</sup> Na<sub>2</sub>SO<sub>4</sub>.

<sup>b</sup> Na<sub>2</sub>NO<sub>3</sub>.

<sup>c</sup> KOH.

<sup>d</sup> NaCl.

spin-energy separation is 11.8 eV. This suggests that the valence state of Mn was +4 [30,31], because these peaks and their spin-energy separation are indicative of the presence of Mn<sub>3</sub>O<sub>4</sub>, which is formed by the conversion of MnO (the primary peaks in the XRD spectra confirm the presence of MnO) into other manganese oxides. This hypothesis is supported by the XRD and Raman data [30]. However, the presence of a satellite feature at 647 eV and the asymmetry of the Mn2p peak indicated that the MnO phase was dominant. The C1s spectrum, shown in Fig. 4c, includes a C–O peak at 286 eV and a C=O peak at 289 eV. In addition, peaks related to sp<sup>2</sup> (C=C) and sp<sup>3</sup> (C–C) carbons are observed at 284.13 and 284.8 eV, respectively. The O1s peak at 530.75 eV (Fig. 4a) indicates that oxygen was present its normal oxidation state of –2. Furthermore, the N1s peaks in the high-resolution spectrum in Fig. 4d provide information about the local bonding environment of nitrogen in the sample. They suggest that N formed a graphitic bond with sp<sup>2</sup> carbon, based on the peak at 400.25 eV, while the peak at 401.25 eV is related to oxidized N.

Transmission electron microscopy (TEM, JEM 2100F, JEOL Inc.) was performed on the sample produced using the optimized amount of MnAc (1 wt%) (i.e., sample MnO-1), as shown in Fig. 5a. TEM shows that the composite consists of CCNFs uniformly embedded with MnO particles. In addition, the selected area electron diffraction (SAED) pattern, shown in the inset of Fig. 5a, is a diffuse ring pattern, suggesting that the MnO particles were crystalline but had a low crystallinity. The diffraction rings could be indexed to the (200) and (220) planes of MnO.

The high-resolution TEM (HRTEM) image in Fig. 5b confirms the formation of MnO crystals and is in keeping with the peaks observed in the XRD spectra (Fig. 2a). The well-resolved lattice fringes in Fig. 5b indicate interplanar spacings of 0.22 and 0.15 nm for the (200) and (220) planes of the cubic MnO phase. The elemental maps for C, Mn, and O are shown in Fig. 5c, showing that the elements are distributed homogeneously on the CCNF. On the other hand, the sites created by the sacrifice of the PMMA during carbonization in the central region are filled with MnO particles. The distribution of elements in MnO-2 and MnO-3 is presented in the supporting information, Fig. S2. With increasing concentration of MnAc (MnO-3) the density of Mn increased whereas the ratio of oxygen to Mn decreased. This may be due to the combined effect of argon gas annealing and presence of carbamide. Among these samples, MnO-1 sample shows a more homogenous distribution of elements.

Cyclic voltammetry (CV) and galvanostatic charge/discharge (GCD) measurements provide deep insights into the characteristics of the electrochemical reactions that occur in symmetric SCs. In addition, based on the CV and GCD curves, one can estimate the

specific capacitance of the electrode material using Eqs. (1) and (2), respectively. When using the CV curve, the capacitance is given by

$$C = \frac{1}{msV} \int_{V-}^{V+} i(V)dV \quad (1)$$

where  $m$  is the mass of the binder-free and freestanding active material in both electrodes ( $g$ ),  $s$  is the scan rate ( $mV \cdot s^{-1}$ ),  $V$  is the capacitive potential range ( $V$ ),  $i(V)$  is the voltage-dependent output current ( $mA$ ), and  $V-$  and  $V+$  are the lower and upper voltages of the capacitive potential range.

In the case of the GCD curve, the specific capacitance is given by the following equations:

$$C_s = \frac{4It_d}{m(V-IR)} \quad (2)$$

$$E = 0.5C_s V^2 \quad (3)$$

$$P = E/t_d \quad (4)$$

where  $C_s$  is the specific capacitance ( $F \cdot g^{-1}$ ),  $I$  is the discharge current ( $A$ ),  $t_d$  is the discharge time ( $s$ ),  $m$  is the combined mass of both electrodes ( $g$ ),  $V$  is the capacitive potential range ( $V$ ), and  $IR$  is the ohmic drop ( $V$ ) during the discharge cycle. The energy density,  $E$  ( $Wh \cdot kg^{-1}$ ), and power density,  $P$  ( $W \cdot kg^{-1}$ ), can be determined using Eq. (3) and (4), respectively [25].

The CV measurements were carried out at different scan rates (2, 5, 10, 20, 30, 50, and 100  $mV \cdot s^{-1}$ ). To allow for clearer visualization, only the CV curves for the scan rates of 10, 30, 50, and 100  $mV \cdot s^{-1}$  are given in Fig. 6a–c. The CV curves show the variation in the current density ( $I_d$   $A \cdot g^{-1}$ ) in the potential window range of –0.3 to 0.7 V. All the CV curves are indicative of a highly reversible redox reaction. The CV curve of MnO-1, shown in Fig. 6a, suggests that its electrochemical response was better than those of MnO-2 (see Fig. 6b) and MnO-3 (see Fig. 6c). The reduced area of the CV curve in the cases of MnO-2 and MnO-3 indicates reduced electrochemical activity, as was also confirmed by electrochemical impedance spectroscopy. Note that the curves for the samples corresponding to the other concentrations of MnAc are shown in Fig. S3.

At a very low scan rate (2  $mV \cdot s^{-1}$ ), in the case of MnO-1, diffusion occurs readily, and the composite sample exhibits a very high specific capacitance (645  $F \cdot g^{-1}$ ). Further, when the scan rate is increased, the MnO-1 electrode continues to show good scan rate ability, with its specific capacitance being 365  $F \cdot g^{-1}$  at a scan rate of 100  $mV \cdot s^{-1}$ . On the other hand, the MnO-2 electrode shows a specific capacitance of 600  $F \cdot g^{-1}$  at a scan rate of 2  $mV \cdot s^{-1}$ , which is reduced to 250  $F \cdot g^{-1}$  at a scan rate of 100  $mV \cdot s^{-1}$ . Further, the MnO-3 electrode show a specific capacitance of 539  $F \cdot g^{-1}$  at a scan rate of 2  $mV \cdot s^{-1}$ ; however, it is reduced to 142  $F \cdot g^{-1}$  at a

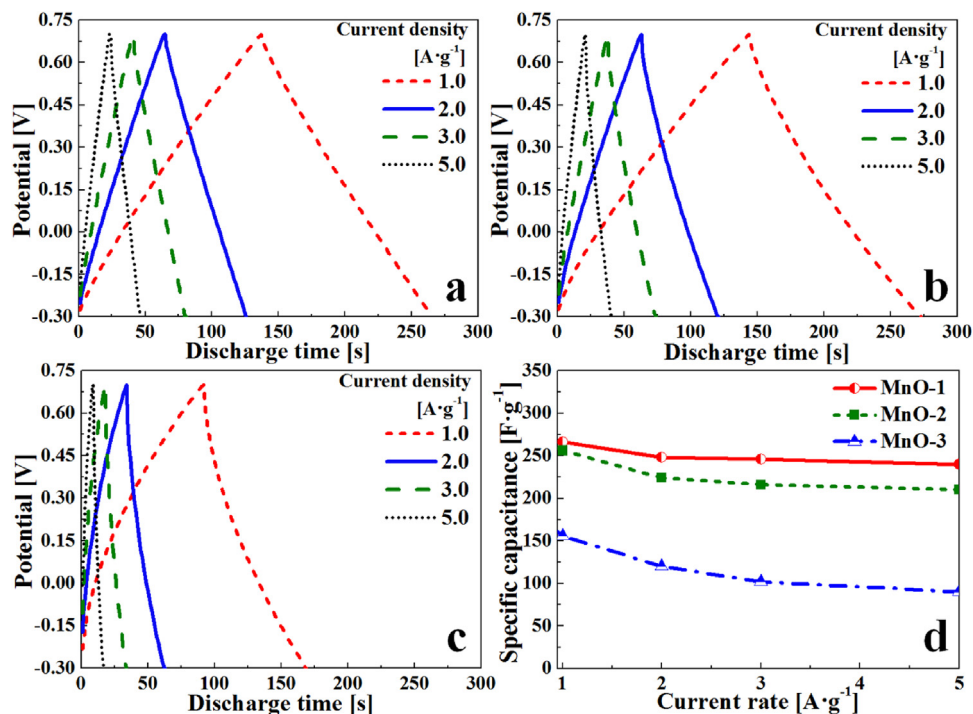


Fig. 7. Galvanostatic charge/discharge curves of (a) MnO-1, (b) MnO-2, and (c) MnO-3 and (d) their gravimetric specific capacitances at different current densities.

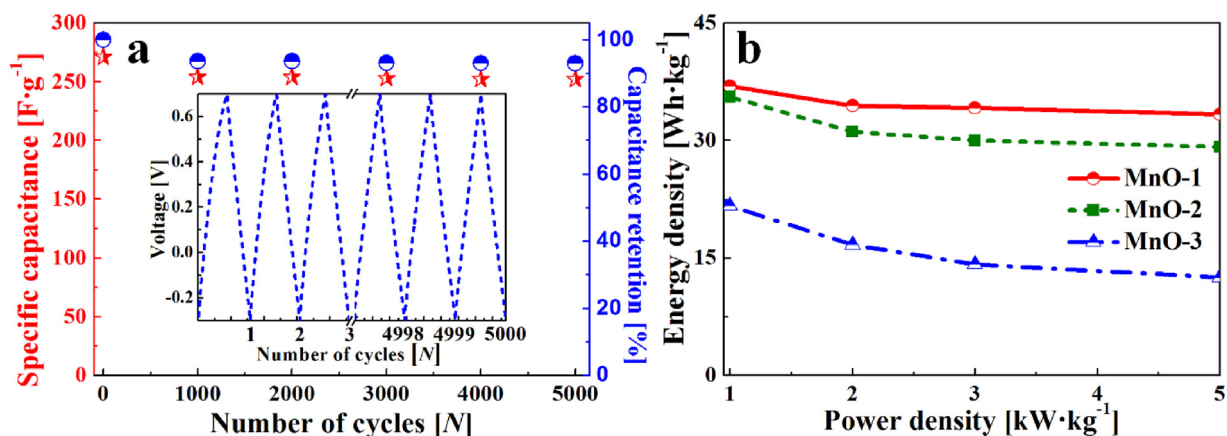
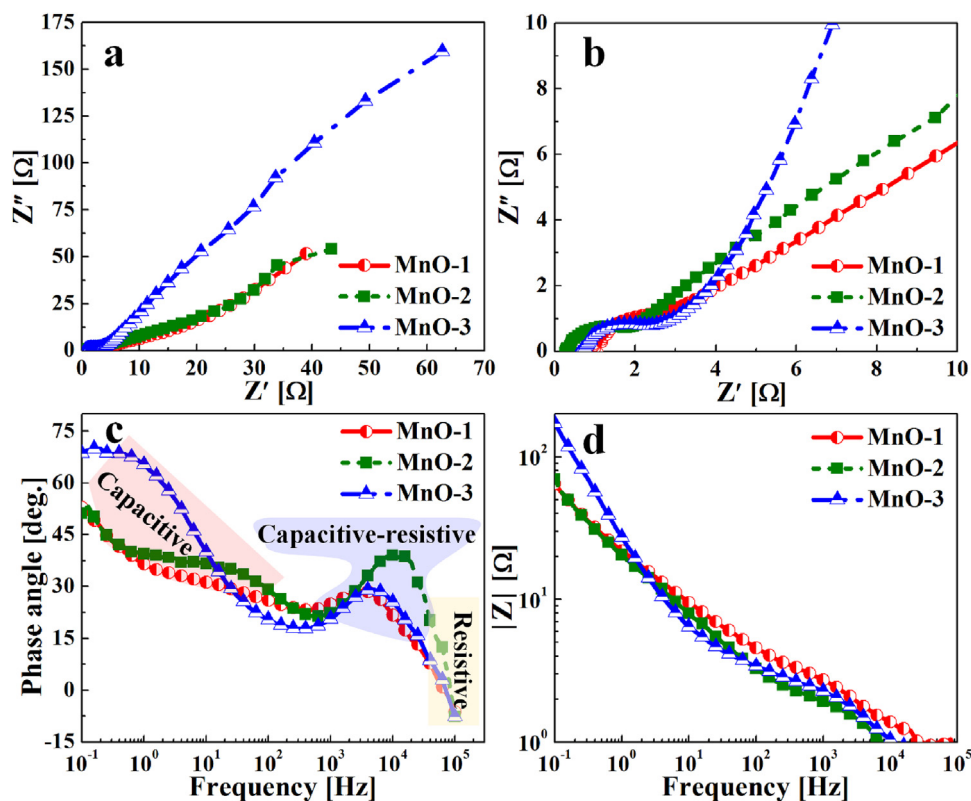


Fig. 8. (a) Long-term specific capacitance (star symbols), retention rate (circles), and galvanostatic charge/discharge curve (inset) of MnO-1. (b) Ragone plots of MnO-1, MnO-2, and MnO-3.

scan rate of  $100 \text{ mV}\cdot\text{s}^{-1}$ . Thus, the MnO-1 sample shows the best capacitance, which is probably owing to the uniform distribution of MnO particles over the CCNFs, as indicated by the elemental TEM maps in Fig. 5c. Note that samples with MnAc concentrations of 0 and 0.5 wt% as well as a pure CCNF sample (0.33 wt% carbamide) were also investigated, as shown in Fig. S3c. In the absence of MnO, the pure CCNF sample exhibited a relatively low current density (Figs. S3a and b). Fig. S3d compares the specific capacitance values of samples MnO-0 and MnO-0.5 and the sample with 0.33 wt% carbamide. It is evident that the inclusion of MnO increases the capacitance, as seen in the case of MnO-0.5. The ultrafine MnO<sub>x</sub> particles in the MnO<sub>x</sub>/CCNF composites contributed to the enhancement in the pseudocapacitance. This was because the ultrafine MnO particles lowered the ion diffusion length, thus aiding the capacitance-related Faradaic redox reactions. On the other hand, the CCNFs ensured high conductivity (as shown in supporting information Fig. S4 and Table S1) and endowed SC characteristics, as evidenced by the rectangular shape of the CV curves. As a result,

the MnO<sub>x</sub>/CCNF composites showed high specific capacitances. The comparison in Table 3 confirms that the MnO-1 electrode exhibited the highest capacitance at the highest scan rate of  $10 \text{ mV}\cdot\text{s}^{-1}$ . The data in Table S2 further support this conclusion, showing that the electrode exhibited a higher retention rate at the highest scan rate ( $10 \text{ mV}\cdot\text{s}^{-1}$ ) compared with similar materials reported previously, with the only exception being the Pt-coated electrode reported by Wang et al. [3].

Fig. 7a–c shows the GCD curves of the MnO-1, MnO-2, and MnO-3 samples. The galvanostatic electrochemical performances were investigated for current densities of 1–5  $\text{A}\cdot\text{g}^{-1}$  in 6 M KOH as the electrolyte. As can be seen from the figures, there was no change in the internal resistance; this confirmed the excellent electrical conductivity of the electrodes. Further, the charge/discharge curves are triangular, indicating that the electrodes were capable of a rapid electrochemical response; this was because of the increased interlayer spacing of carbon, which increased the electrical conductivity (see Fig. 2a). The specific capacitances of MnO-1, MnO-2, and MnO-



**Fig. 9.** Results of electrochemical impedance spectroscopy analysis of  $\text{MnO}_x/\text{CCNF}$  composite samples: (a) Nyquist plots and (b) magnified versions of Nyquist plots. Frequency-dependent Bode plots showing (c) phase angle and (d) modulus of impedance responses of different composite samples.

3 for the potential window of  $-0.3$  to  $0.7$  V are shown in Fig. 7d. MnO-1 and MnO-2 showed high capacitances of  $266$  and  $256 \text{ F}\cdot\text{g}^{-1}$ , respectively, at a current density of  $1 \text{ A}\cdot\text{g}^{-1}$ . However, at a higher current density ( $5 \text{ A}\cdot\text{g}^{-1}$ ), the specific capacitances were reduced to  $240$  and  $210 \text{ F}\cdot\text{g}^{-1}$ , respectively. These values are  $90$  and  $82\%$  of the initial values for MnO-1 and MnO-2, respectively. Further, MnO-3 showed the lowest specific capacitance, with the charge/discharge curves for this sample, which was formed using a higher MnAc concentration, being irregular (see Fig. 7c).

SCs are attracting a lot of interest because they fill the gap between aluminum electrolytic capacitors and batteries. Further, SCs exhibit higher energy densities than do capacitors and show significantly higher power densities than those of batteries. Hence, to confirm the suitability of the synthesized composites as electrode materials for SCs, their galvanostatic charging/discharging performances were analyzed, and their Ragone curves were plotted based on the obtained data to elucidate the relationship between their energy and power densities. Fig. 8a shows the long-term galvanostatic charging/discharging performance of MnO-1 in terms of the changes in its specific capacitance with cycling ( $N=5000$ ) as well as its retention ability. Its specific capacitance varied from  $271 \text{ F}\cdot\text{g}^{-1}$  for  $N=1$  to  $252 \text{ F}\cdot\text{g}^{-1}$  for  $N=5000$  at a current density of  $1 \text{ A}\cdot\text{g}^{-1}$ . Further, the retention rate of MnO-1 was  $93\%$  during galvanostatic charging/discharging. The inset of Fig. 8a shows that the charge/discharge curve remained triangular and symmetric. Thus, it can be concluded that the flexible MnO-1 electrode underwent reversible reactions during long-term cycling. Fig. 8b shows that it exhibited an energy density of  $33 \text{ Wh}\cdot\text{kg}^{-1}$  and power density of  $5 \text{ kW}\cdot\text{kg}^{-1}$  at a galvanostatic current density of  $5 \text{ A}\cdot\text{g}^{-1}$ . For a lower current density ( $1 \text{ A}\cdot\text{g}^{-1}$ ), its energy and power densities were  $37 \text{ Wh}\cdot\text{kg}^{-1}$  and  $1 \text{ kW}\cdot\text{kg}^{-1}$  respectively. The increase in the energy density at the lower current density was due to the greater utilization of the available electroactive surface area. At lower rates,

the electrolyte ions have more time to diffuse to the entire available surface area.

Fig. S5 shows the CV curves of MnO-1 corresponding to long-term cycling. The curves do not exhibit any redox-reaction-related peaks and maintain their quasi-rectangular shape, highlighting the excellent performance of the SC electrode. The CV curves were obtained at a scan rate of  $10 \text{ mV}\cdot\text{s}^{-1}$ , with the electrode showing a retention rate of  $106\%$ . That is to say, there was an increase of  $6\%$  in its specific capacitance from  $468 \text{ F}\cdot\text{g}^{-1}$  for  $N=1$  to  $496 \text{ F}\cdot\text{g}^{-1}$  for  $N=5000$ . Fig. S5 shows that the variation between the  $1000$ th cycle and the  $5000$ th cycle was minimal, thus confirming that the electrode showed highly stable performance, primarily owing to the synergistic effects of carbon and MnO. Finally, the capacitance retention performance of the electrode material is compared to those of other similar materials reported previously in Table S2.

The electrochemical performances of the  $\text{MnO}_x/\text{CCNF}$  composite samples, as they relate to their pseudocapacitance, was evaluated using electrochemical impedance spectroscopy. Fig. 9a shows the Nyquist plots of symmetric SCs based on the various  $\text{MnO}_x/\text{CCNF}$  composite samples. Fig. 9b shows magnified versions of the Nyquist plots, which were used to analyze the Warburg impedance-related semicircles in the high-to-medium frequency range. At lower frequencies, the imaginary impedance increases much faster than the real impedance, owing to the capacitive characteristics of the electrodes. The Warburg impedance-related semicircle intercepts the  $x$ -axis, which represents the real impedance, indicating that it is characteristic of the resistance ( $R_s$ ) of the electrolyte solution. The charge-transfer resistance between the electrolyte and the electrode is designated as  $R_{ct}$ . It can be seen from Fig. 9b that, for MnO-1, MnO-2, and MnO-3, the values of  $R_s$  were  $0.88$ ,  $0.31$ , and  $0.75 \Omega$ , respectively, while the calculated  $R_{ct}$  values were  $1.07$ ,  $3.30$ , and  $1.45 \Omega$ , respectively. A smaller  $R_{ct}$  corresponds to a higher power density in SCs [32,33]. The lower charge transfer resistance signif-

icantly contributes to the CV curves of MnO-1 being closer to ideal EDLC characteristics compared to MnO-2 or MnO-3 [34].

As can be seen from the Bode plots in Fig. 9c, the phase angle for MnO-3 is higher in the low-frequency range, indicating that the probability of diffusion is higher in this case. However, the response of this composite sample in the medium-to-high frequency range and its Nyquist plot (Fig. 9a) suggested that its large impedance hindered its capacitive performance. In addition, the area under the region of the curve corresponding to its resistive and capacitive-resistive properties is large, owing to which its specific capacitance, as determined from the CV and GCD curves, is lower.

#### 4. Conclusions

We synthesized a novel MnO<sub>x</sub>/CCNF composite by a one-step electrospinning method for use as a SC electrode material. The composite was formed by the simultaneous decomposition of manganese acetate, carbonization of polyacrylonitrile and carbamide, and pyrolysis of polymethylmethacrylate. The inclusion of carbamide increased the electrical conductivity and hence the SC performance of the composite. The MnAc/carbamide concentration ratio was optimized to ensure both high flexibility and conductivity. As a result, the composite could be used to produce high-performance flexible and freestanding SCs. This one-step electrospinning method is highly scalable and should aid the development of large-scale and commercially viable high-performance SCs.

#### Acknowledgement

This research was supported by Global Frontier Program through the Global Frontier Hybrid Interface Materials (GFHIM) of the NRF-2013M3A6B1078879, NRF-2017R1A2B4005639, and NRF-2016M1A2A2936760.

#### Appendix A. Supplementary data

Supplementary data associated with this article can be found, in the online version, at <http://dx.doi.org/10.1016/j.apsusc.2017.06.098>.

#### References

- [1] Y. Yang, F. Yang, S. Lee, X. Li, H. Zhao, Y. Wang, S. Hao, X. Zhang, Facile fabrication of MnO<sub>x</sub> and N co-doped hierarchically porous carbon microspheres for high-performance supercapacitors, *Electrochim. Acta* 191 (2016) 1018–1025.
- [2] Q. Ke, J. Wang, Graphene-based materials for supercapacitor electrodes - A review, *J. Materiomics* 2 (2016) 37–54.
- [3] Y. Ding, J. Yang, G. Yang, P. Li, Fabrication of ordered mesoporous carbons anchored with MnO nanoparticles through dual-templating approach for supercapacitors, *Ceram. Int.* 41 (2015) 9980–9987.
- [4] M. Zhi, C. Xiang, J. Li, M. Li, N. Wu, Nanostructured carbon-metal oxide composite electrodes for supercapacitors: a review, *Nanoscale* 5 (2013) 72–88.
- [5] W. Cai, Z. Xiong, T. Hussain, J. Yang, Y. Wang, J. Liu, Porous MnO<sub>x</sub> covered electrospun carbon nanofiber for capacitive deionization, *J. Electrochem. Soc.* 163 (2016) A2515–A2523.
- [6] H. Jiang, P.S. Lee, C. Li, 3D carbon based nanostructures for advanced supercapacitors, *Energy Environ. Sci.* 6 (2013) 41–53.
- [7] Y. Li, H. Fu, Y. Zhang, Z. Wang, X. Li, Kirkendall effect induced one-step fabrication of tubular Ag/MnO<sub>x</sub> nanocomposites for supercapacitor application, *J. Phys. Chem. C* 118 (2014) 6604–6611.
- [8] A. González, E. Goikolea, J.A. Barrena, R. Mysyk, Review on supercapacitors: technologies and materials, *Renew. Sustain. Energy Rev.* 58 (2016) 1189–1206.
- [9] X.G. Xiaoping Cheng, Zhiqiang Lin, Yongjia Zheng, Ming Liu, Runze Zhan, Yuan Zhu, Zikang Tang, Three-dimensional α-Fe<sub>2</sub>O<sub>3</sub>/carbon nanotube sponges as flexible supercapacitor electrodes, *J. Mater. Chem. A* 3 (2015) 20927–20934.
- [10] S. Byun, B. Shin, Densely packed hybrid films comprising SnO<sub>2</sub> and reduced graphite oxide for high-density electrochemical capacitors, *J. Mater. Chem. A* 4 (2016) 16175–16183.
- [11] N. Sinan, E. Unur, Fe<sub>3</sub>O<sub>4</sub>/carbon nanocomposite: investigation of capacitive & magnetic properties for supercapacitor applications, *Mater. Chem. Phys.* 183 (2016) 571–579.
- [12] Y. Zou, I.A. Kinloch, R.A. Dryfe, Mesoporous vertical Co<sub>3</sub>O<sub>4</sub> nanosheet array on nitrogen-doped graphene foam with enhanced charge-storage performance, *ACS Appl. Mater. Interfaces* 7 (2015) 22831–22838.
- [13] J.-W. Jung, C.-L. Lee, S. Yu, I.-D. Kim, Electrospun nanofibers as a platform for advanced secondary batteries: a comprehensive review, *J. Mater. Chem. A* 4 (2016) 703–750.
- [14] S. Peng, L. Li, J. Kong, Y. Lee, L. Tian, M. Srinivasan, S. Adams, S. Ramakrishna, Electrospun carbon nanofibers and their hybrid composites as advanced materials for energy conversion and storage, *Nano Energy* 22 (2016) 361–395.
- [15] R. Kötz, M. Carlen, Principles and applications of electrochemical capacitors, *Electrochim. Acta* 45 (2000) 2483–2498.
- [16] J.G. Wang, Y. Yang, Z.H. Huang, F. Kang, Synthesis and electrochemical performance of MnO<sub>2</sub>/CNTs-embedded carbon nanofibers nanocomposites for supercapacitors, *Electrochim. Acta* 75 (2012) 213–219.
- [17] J. Yang, X. Yang, Y.L. Zhong, J.Y. Ying, Porous MnO/Mn<sub>3</sub>O<sub>4</sub> nanocomposites for electrochemical energy storage, *Nano Energy* 13 (2015) 702–708.
- [18] G. Nie, X. Lu, J. Lei, C. Wang, Seed-assisted synthesis of hierarchical manganese dioxide/carbonaceous sphere composites with enhanced supercapacitor performance, *Electrochim. Acta* 180 (2015) 1033–1040.
- [19] D. Liu, X. Zhang, T. You, Urea-treated carbon nanofibers as efficient catalytic materials for oxygen reduction reaction, *J. Power Sour.* 273 (2015) 810–815.
- [20] S. Ci, Z. Wen, Y. Qian, S. Mao, S. Cui, J. Chen, NiO-Microflower formed by nanowire-weaving nanosheets with interconnected Ni-network decoration as supercapacitor electrode, *Sci. Rep.* 5 (2015) 11919.
- [21] R. Chen, Y. Hu, Z. Shen, Y. Chen, X. He, X. Zhang, Y. Zhang, Controlled synthesis of carbon nanofibers anchored with Zn<sub>3</sub>Co<sub>3-x</sub>O<sub>4</sub> nanocubes as binder-free anode materials for lithium-ion batteries, *ACS Appl. Mater. Interfaces* 8 (2016) 2591–2599.
- [22] A.V. Bazilevsky, A.L. Yarin, C.M. Megaridis, Co-electrospinning of core-shell fibers using a single-nozzle technique, *Langmuir* 23 (2007) 2311–2314.
- [23] C. Kim, Y.I. Jeong, B.T. Ngoc, K.S. Yang, M. Kojima, Y.A. Kim, M. Endo, J.W. Lee, Synthesis and characterization of porous carbon nanofibers with hollow cores through the thermal treatment of electrospun copolymeric nanofiber webs, *Small* 3 (2007) 91–95.
- [24] B.N. Joshi, S. An, H.S. Jo, K.Y. Song, H.G. Park, S. Hwang, S.S. Al-Deyab, W.Y. Yoon, S.S. Yoon, Flexible, freestanding, and binder-free SnO<sub>x</sub>-ZnO/carbon nanofiber composites for lithium ion battery anodes, *ACS Appl. Mater. Interfaces* 8 (2016) 9446–9453.
- [25] L. Liu, J. Lang, P. Zhang, B. Hu, X. Yan, Facile synthesis of Fe<sub>2</sub>O<sub>3</sub> nano-Dots@Nitrogen-Doped graphene for supercapacitor electrode with ultralong cycle life in KOH electrolyte, *ACS Appl. Mater. Interfaces* 8 (2016) 9335–9344.
- [26] X. Mao, X. Yang, J. Wu, W. Tian, G.C. Rutledge, T.A. Hatton, Microwave-assisted oxidation of electrospun turbostratic carbon nanofibers for tailoring energy storage capabilities, *Chem. Mater.* 27 (2015) 4574–4585.
- [27] J. Yan, Z. Fan, T. Wei, W. Qian, M. Zhang, F. Wei, Fast and reversible surface redox reaction of graphene-MnO<sub>2</sub> composites as supercapacitor electrodes, *Carbon* 48 (2010) 3825–3833.
- [28] C. Zhu, C.g. Han, G. Saito, T. Akiyama, MnO nanocrystals incorporated in a N-containing carbon matrix for Li ion battery anodes, *RSC Adv.* 6 (2016) 30445–30453.
- [29] J. Chang, M. Jin, F. Yao, T.H. Kim, V.T. Le, H. Yue, F. Gunes, B. Li, A. Ghosh, S. Xie, Y.H. Lee, Asymmetric supercapacitors based on Graphene/MnO<sub>2</sub> nanospheres and graphene/MoO<sub>3</sub> nanosheets with high energy density, *Adv. Funct. Mater.* 23 (2013) 5074–5083.
- [30] S. He, W. Chen, Application of biomass-derived flexible carbon cloth coated with MnO<sub>2</sub> nanosheets in supercapacitors, *J. Power Sour.* 294 (2015) 150–158.
- [31] L. Qiao, M.T. Swihart, Solution-phase synthesis of transition metal oxide nanocrystals: morphologies, formulae, and mechanisms, *Adv. Colloid Interface Sci.* (2016), <http://dx.doi.org/10.1016/j.cis.2016.01.005>.
- [32] D. Antiohos, K. Pingmuang, M.S. Romano, S. Beirne, T. Romeo, P. Aitchison, A. Minett, G. Wallace, S. Phanichphant, J. Chen, Manganosite-microwave exfoliated graphene oxide composites for asymmetric supercapacitor device applications, *Electrochim. Acta* 101 (2013) 99–108.
- [33] S. Deng, D. Sun, C. Wu, H. Wang, J. Liu, Y. Sun, H. Yan, Synthesis and electrochemical properties of MnO<sub>2</sub> nanorods/graphene composites for supercapacitor applications, *Electrochim. Acta* 111 (2013) 707–712.
- [34] J. Du, D. Mishra, J.M. Ting, Surface modified carbon cloth for use in electrochemical capacitor, *Appl. Surf. Sci.* 285 (2013) 483–489.
- [35] J.G. Wang, Y. Yang, Z.H. Huang, F. Kang, Effect of temperature on the pseudo-capacitive behavior of freestanding MnO<sub>2</sub>@carbon nanofibers composites electrodes in mild electrolyte, *J. Power Sour.* 224 (2013) 86–92.
- [36] Y. Zhao, Y. Meng, P. Jiang, Carbon@MnO<sub>2</sub> core-shell nanospheres for flexible high-performance supercapacitor electrode materials, *J. Power Sour.* 259 (2014) 219–226.
- [37] X.-Y. Zhang, L.-Q. Han, S. Sun, C.-Y. Wang, M.-M. Chen, MnO<sub>2</sub>/C composite electrodes free of conductive enhancer for supercapacitors, *J. Alloys Compd.* 653 (2015) 539–545.
- [38] Y. Li, Y. Mei, L.Q. Zhang, J.H. Wang, A.R. Liu, Y.J. Zhang, S.Q. Liu, Manganese oxide nanowires wrapped with nitrogen doped carbon layers for high performance supercapacitors, *J. Colloid Interface Sci.* 455 (2015) 188–193.